LETTERS
PUBLISHED ONLINE: 25 OCTOBER 2017 | DOI: 10.1038/NMAT5007
nature materials

Emergent dynamic chirality in a thermally driven artificial spin ratchet

Sebastian Gliga[1,2,3]*, Gino Hrkac[4], Claire Donnelly[2,3], Jonathan Büchi[2], Armin Kleibert[3], Jizhai Cui[2,3], Alan Farhan[2,3,5], Eugenie Kirk[2,3], Rajesh V. Chopdekar[6], Yusuke Masaki[7], Nicholas S. Bingham[2,3,8], Andreas Scholl[5], Robert L. Stamps[1] and Laura J. Heyderman[2,3]

Modern nanofabrication techniques have opened the possibility to create novel functional materials, whose properties transcend those of their constituent elements. In particular, tuning the magnetostatic interactions in geometrically frustrated arrangements of nanoelements called artificial spin ice[1,2] can lead to specific collective behaviour[3], including emergent magnetic monopoles[4,5], charge screening[6,7] and transport[8,9], as well as magnonic response[10–12]. Here, we demonstrate a spin-ice-based active material in which energy is converted into unidirectional dynamics. Using X-ray photoemission electron microscopy we show that the collective rotation of the average magnetization proceeds in a unique sense during thermal relaxation. Our simulations demonstrate that this emergent chiral behaviour is driven by the topology of the magnetostatic field at the edges of the nanomagnet array, resulting in an asymmetric energy landscape. In addition, a bias field can be used to modify the sense of rotation of the average magnetization. This opens the possibility of implementing a magnetic Brownian ratchet[13,14], which may find applications in novel nanoscale devices, such as magnetic nanomotors, actuators, sensors or memory cells.

Chirality is a ubiquitous phenomenon in nature present in a variety of systems, from elementary particles, through the charge-parity violation of the weak interaction, to biomolecules whose function is defined by their handedness. In artificial systems, such as optical metamaterials, structural chirality can be exploited to control light–matter interactions and produce circularly polarized light[15]. In ferromagnets and antiferromagnets, the Dzyaloshinskii–Moriya interaction can give rise to chiral spin textures[16] and lead to non-reciprocal dynamics[17]. Although most studied phenomena rely on a static view of chirality, based on whether the system is superimposable on its mirror image, the definition of chirality can be extended to include electric and magnetic fields as well as dynamic properties[18]. In this context, dynamic chirality is a property of both chiral as well as achiral objects that display a preferred sense of rotation. In classical mechanics, an example is the rattleback: a spinning top that only rotates in one direction, while in chemistry, the interactions between an adsorbed molecule and a crystal surface can lead to the rotation of the molecule in a preferred direction[19].

Here we present an example of emergent dynamic chirality in an artificial spin ice system—a 'chiral ice'. Schematically represented in Fig. 1, the system consists of a two-dimensional arrangement of lithographically patterned single-domain nanomagnets in which the magnetization points in one of two orientations along the magnet long axis due to shape anisotropy[1]. The choice of the array design is such that it is structurally chiral—that is, it cannot be superimposed onto its mirror image—when considering the edges of the array. The two-dimensional character of the system is constrained by the shape anisotropy of the nanomagnets (see Methods). Each vertex is associated with four nanomagnets oriented at an angle of 90° with respect to each other and the net magnetization, $\mathbf{M}_v$, is the sum of the magnetization, $\mathbf{M}$, of the individual elements at a vertex. We observe that, after applying and removing a sufficiently large external field to saturate the array (see Methods), the thermally activated relaxation at room temperature is characterized by the rotation of the net magnetization at the individual vertices in a unique direction: from state A to state B, as illustrated in Fig. 1. No statistically significant fraction of the vertices evolves from state A to state D, thus defining a ratchet in which the energy supplied by the saturating field is transformed into the clockwise rotation of the average magnetization. This is a realization of active matter: an out-of-equilibrium system that locally converts energy into directed motion[20,21]. In thermal equilibrium a preferred direction of rotation does not occur due to microscopic reversibility. However, chiral evolution is possible if the system is far from equilibrium and in the presence of an asymmetric potential[22]. Using micromagnetic simulations, we find that an asymmetry is indeed generated in our system as a result of the topology of the stray field of the nanomagnet array. At the edges of the array, the stray field gives rise to emergent patterns, whose specific rearrangement during the thermal evolution can decrease the energy of the system, reminiscent of the role of magnetic surface charges in a ferromagnet. It is the energy decrease that accompanies the reordering of these 'emergent charges' that drives the chiral dynamics of the system during the thermal relaxation. Moreover, in the presence of a small bias field, heating allows the vertices to evolve into state C (Fig. 1).

The experimental system consists of a finite array of elongated Permalloy nanomagnets arranged on a square grid, as shown in Fig. 2a. An image of the full array is shown in Supplementary Information 1. We combine photoemission electron microscopy (PEEM) with X-ray magnetic circular dichroism (XMCD) to image

[1]SUPA, School of Physics and Astronomy, University of Glasgow, Glasgow G12 8QQ, UK. [2]Laboratory for Mesoscopic Systems, Department of Materials, ETH Zurich, 8093 Zurich, Switzerland. [3]Paul Scherrer Institut, 5232 Villigen PSI, Switzerland. [4]College of Engineering, Mathematics and Physical Sciences, University of Exeter, Exeter EX4 4QF, UK. [5]Advanced Light Source, Lawrence Berkeley National Laboratory (LBNL), 1 Cyclotron Road, Berkeley, California 94720, USA. [6]Department of Materials Science and Engineering, University of California, Davis, Davis, California 95616, USA. [7]Department of Physics, University of Tokyo, Tokyo 113-0033, Japan. [8]National Research Council Research Associate at the US Naval Research Laboratory, 4555 Overlook Avenue, SW Washington DC 20375, USA. *e-mail: sebastian.gliga@glasgow.ac.uk

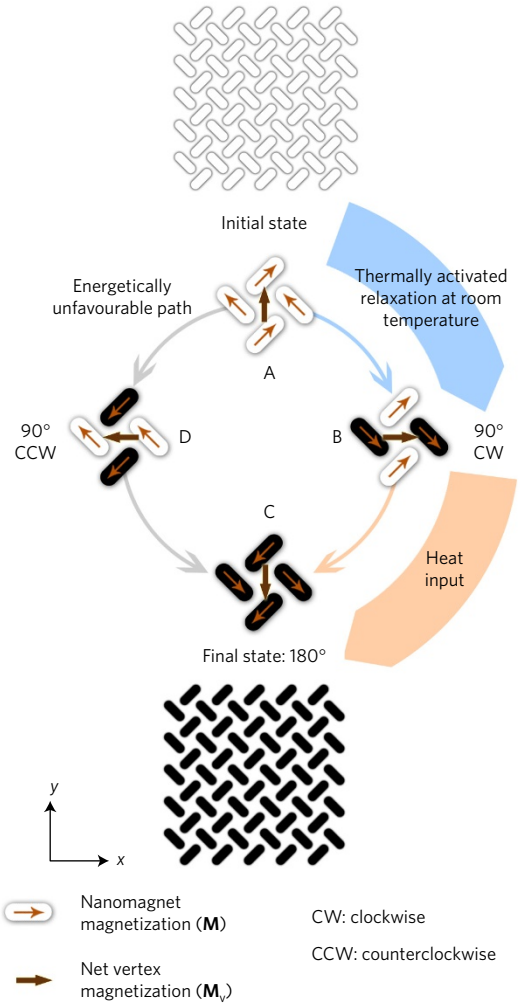

Figure 1 | Schematic representation of the chiral ice and evolution of the net magnetization at individual vertices within the array. The thermally activated evolution after initial saturation along the $+y$ direction (state A) is illustrated, with the white or black colour, respectively, indicating the direction of the magnetization **M** toward the positive or negative y axis. The thin orange arrows represent the magnetization within the nanomagnets while the net magnetization at each individual vertex, $\mathbf{M}_v$, is indicated by the large brown arrows. The thermal relaxation at room temperature takes place stepwise via a clockwise rotation of the net magnetization by 90° to state B and is indicated by the blue arrows. When the system is heated above room temperature in the presence of a bias field, the average magnetization can locally rotate further (orange arrows), to state C. Considering the evolution from state A, state D statistically occurs with very low probability. The net vertex magnetization therefore consistently rotates clockwise.

the magnetic state of the individual nanomagnets. In the XMCD images (Fig. 2b), the nanomagnets in which the magnetization points towards the propagation direction of the X-rays display a bright contrast, whereas nanomagnets in which the magnetization is reversed display a dark contrast. The homogeneous XMCD contrast for each nanomagnet confirms that they are in a single-domain state. The nanomagnets are sufficiently thin (see Methods), such that thermal energy can overcome the energy barrier to switch between the two possible single-domain states at room temperature. The thickness is chosen so that the switching rates are comparable to the PEEM measurement timescale[23,24]. We first apply a saturating magnetic field, $\mathbf{H}_{sat}$ (see Methods), such that, after its removal, the average remanent magnetization of the array points along the positive y direction (Fig. 2c, where all nanomagnets display a bright contrast). The measured time evolution of the magnetization over a period of 21 h is shown in Fig. 2d–h in the presence of a weak bias field, as indicated in Fig. 2 (see Methods). The formation of regions with a 'chequerboard' magnetic contrast pattern observed in Fig. 2d indicates that the average magnetization at these vertices has evolved from state A to state B (see also Fig. 2b for a detailed view of state B), and has hence rotated by 90° in the clockwise direction. The evolution slows down considerably after about 4 h, indicating that the system approaches thermal equilibrium, as explained in Supplementary Information 2. Heating the sample by a few kelvin ensures that the thermal evolution, and therefore the rotation of vertices from state A to B, continues while vertices already in state B evolve into state C (dark contrast regions in Fig. 2e, where the net magnetization has locally rotated by 180°). Throughout the evolution, the rotation of the net vertex magnetization $\mathbf{M}_v$ (see Fig. 2b) starts at the edges of the array and propagates towards its centre. The heat-assisted rotation continues until the magnetization in the array has mostly rotated by 180° with respect to state A (Fig. 2h). The quantitative evolution of the different vertex types (A, B and C) as well as the heating schedule are shown in Supplementary Information 3.

To confirm that the observed chiral behaviour is a magnetostatically driven effect, we performed similar measurements on systems with a larger relative distance between nanomagnets, in which the strength of the magnetostatic interaction was therefore reduced, and found that the thermal evolution became achiral (see Supplementary Information 4). We also note that we did not observe any preferred direction of rotation in structures consisting of a single vertex with four nanomagnets, despite their structural chirality. A chiral structure by itself is therefore not sufficient to generate the observed dynamics: in the following we show that the dynamics is driven by the existence of an emergent asymmetric magnetostatic energy landscape.

We performed micromagnetic simulations to qualitatively understand why the clockwise evolution of the magnetization is favoured over the counterclockwise evolution. The simulated system is a finite system identical to the one shown in Fig. 1, with the same overall geometry as the experimentally studied one, but with fewer magnets due to the computational cost of simulating the entire experimental array (see Methods). We consider the system without the bias field to determine its intrinsic thermal behaviour. Figure 3a is a close-up of a section of the simulated array, following saturation and removal of the field $\mathbf{H}_{sat}$ (equivalent to state A in Fig. 2). The magnetostatic volume charge density, $\rho = -\mu_0(\nabla \cdot \mathbf{M})$, is plotted inside the nanomagnets along with the generated stray field outside the nanomagnets. The stray field displays a complex topology owing to the presence of antivortex patterns. Antivortices are two-dimensional structures characterized by a field distribution in which the direction of the field revolves around a central point[25]. An antivortex is schematically illustrated in the inset of Fig. 3a, where the centre of the structure is indicated with an orange dot. Because antivortices typically occur inside ferromagnets, we refer to the observed stray field patterns as virtual antivortices—that is, whose centre is located outside the nanomagnets[26]. Such virtual structures have previously been reported to play a role in the stability of magnetization patterns[25] as well as in the dynamics of coupled systems[27]. Considering the entire simulated array (Fig. 3b), the distribution of the virtual antivortices within the system following saturation is plotted in Fig. 3c. The overall stray field topology effectively forms a virtual antivortex crystal, displaying an ordered arrangement within the bulk of the array. At the edges, the distribution of the virtual antivortices breaks the symmetry of the bulk arrangement. Moreover, their distribution along the horizontal edges (top and bottom; highlighted in blue) and along the vertical edges (left and right; highlighted in red) is

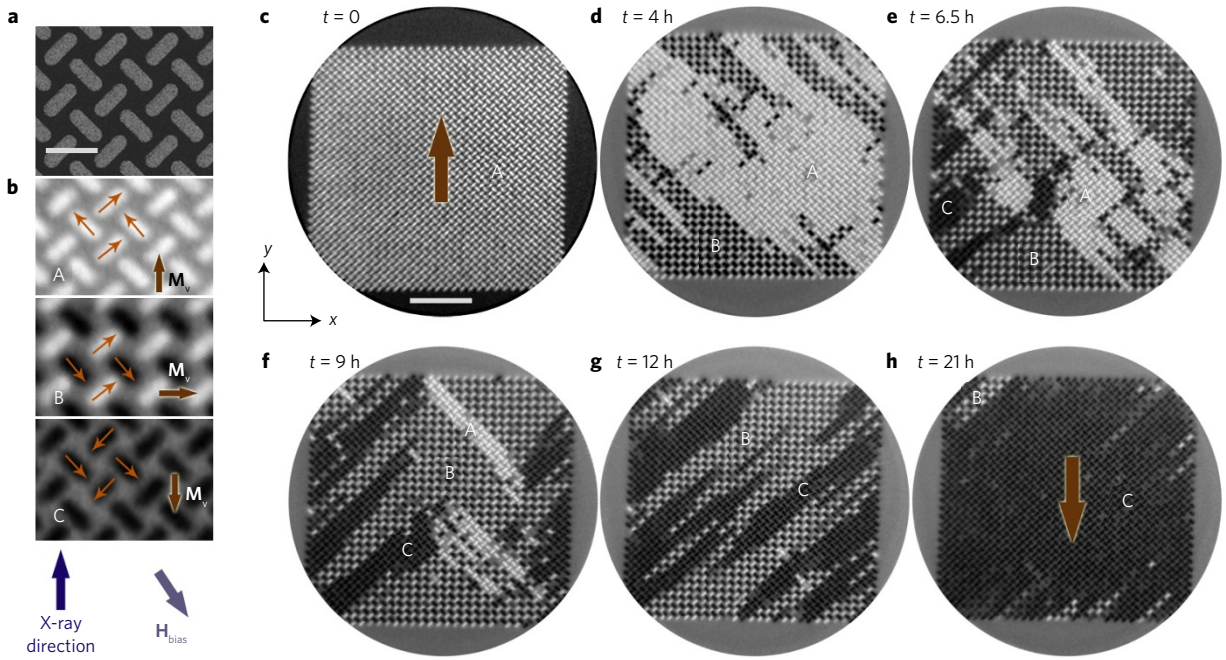

Figure 2 | Measured clockwise evolution of the magnetization following saturation along the +*y* direction. a, Scanning electron microscopy (SEM) image of a region of the investigated array. The scale bar represents 600 nm. **b**, XMCD contrast for states A, B and C, with arrows showing the orientation of the magnetization for selected nanomagnets and the net vertex magnetization in each case indicated with a larger brown arrow and denoted $\mathbf{M}_v$. **c**, XMCD image of the array following saturation along the $+y$ direction. The vertices are in state A with the average magnetization within the array indicated by the large brown arrow. The detailed magnetic configuration of state A is shown in **b**. The scalebar represents 5 μm and the field of view is of 25 μm. The contrast was adjusted for better visibility. **d**–**h**, Time evolution of the magnetization in the presence of a bias field. The magnitude of $\mathbf{H}_{bias}$ is between 50 μT and 80 μT, in the indicated direction. In **d**, thermal relaxation at room temperature gives rise to domains of vertices in state B, mainly nucleating from the array edges. The detailed magnetic configuration of state B is shown in **b**. The sample temperature was subsequently increased by a few kelvin for four hours to ensure that the magnetization reversals continue, as seen in **e**–**g**. In **e**, domains of vertices in state C (shown in **b**) nucleate from the edges of the array. Around $t = 15$ h, the sample was heated again to achieve a close-to-complete 180° reversal of the magnetization, observed in **h**.

different. The virtual antivortex distribution for a partial clockwise rotation of the vertex magnetization by 90° (state B) along four diagonals of the array is given in Fig. 3d. This corresponds to the magnetic state labelled 'CW,1' (CW with edge configuration 1) in Fig. 3f, where the four diagonals can be seen, and is representative of experimentally observed configurations. Within the bulk of the simulated array, the arrangement of the virtual antivortices is modified: in domains where the net vertex magnetization has rotated by 90° (dark grey regions), the antivortex stray field patterns are also rotated by 90°. At the edges of such domains (light grey regions), the antivortices are rotated by 45°, mirroring the rotation of the average magnetization of those vertices. However, it is the changes along the edges that are key to the chiral evolution: although the number of virtual antivortices remains constant, they have been rearranged compared to Fig. 3c. This is analogous to the situation in a finite-sized ferromagnet, where the stray field energy can be minimized through the rearrangement of surface charges, whose density is given by $\sigma = \mu_0(\mathbf{M} \cdot \mathbf{n})$ (where $\mathbf{n}$ is an outward normal vector to the surface) and result in the formation of domains within the ferromagnet. The rearrangement of the virtual antivortices in alternating patterns along the array edges is thus reminiscent of the pole avoidance principle in ferromagnets, which leads to the minimization of the magnetostatic energy through a reduction of the total magnetic charge. In the studied system, the virtual antivortices thus function as emergent surface charges whose rearrangement, through the rotation of the magnetization, minimizes the total energy of the system during relaxation. In Fig. 3e, the emergent charge distribution is given for a system with four diagonals along which the average magnetization has rotated counterclockwise. This distribution corresponds to the magnetic state labelled 'CCW,1' (CCW with edge configuration 1) in Fig. 3f, where the vertices along those diagonals are in state D (see Fig. 1 for state D). When compared to Fig. 3d, the overall virtual antivortex structure is generally mirrored (along an axis defined by the saturation direction, y), except at the edges, where their distribution is not mirrored. Our simulations show that these differences lead to an asymmetric energy landscape in which the energy of the system decreases more efficiently through the clockwise rotation of the net vertex magnetization at the edges than through the counterclockwise rotation. We plot in Fig. 3f the normalized energy barriers at 300 K between the initial state (Fig. 3c) and the states in Fig. 3d,e (which are labelled as 'CW,1' and 'CCW,1', respectively). The energy barrier to access the clockwise state is lower, thus making it more probable. The energy barriers are also plotted for configurations in which nanomagnets at the edges of the array have not switched. We find that, in these cases, the energy barriers for the clockwise and counterclockwise rotations of the net vertex magnetization become equal. These results demonstrate that the chiral behaviour is driven by the edges of the system and that the observed initial clockwise rotation of the net vertex magnetization following saturation is due to the intrinsically asymmetric energy landscape of the system.

The evolution of the average magnetization during relaxation at room temperature eventually leads to thermal equilibrium. The measured continuous clockwise evolution of the magnetization in the experiment towards state C is thus enabled by the bias field, which effectively modifies the energy landscape, such that the system can access state C upon moderate heating. We have also found that the bias field can, in some cases, be used to reverse

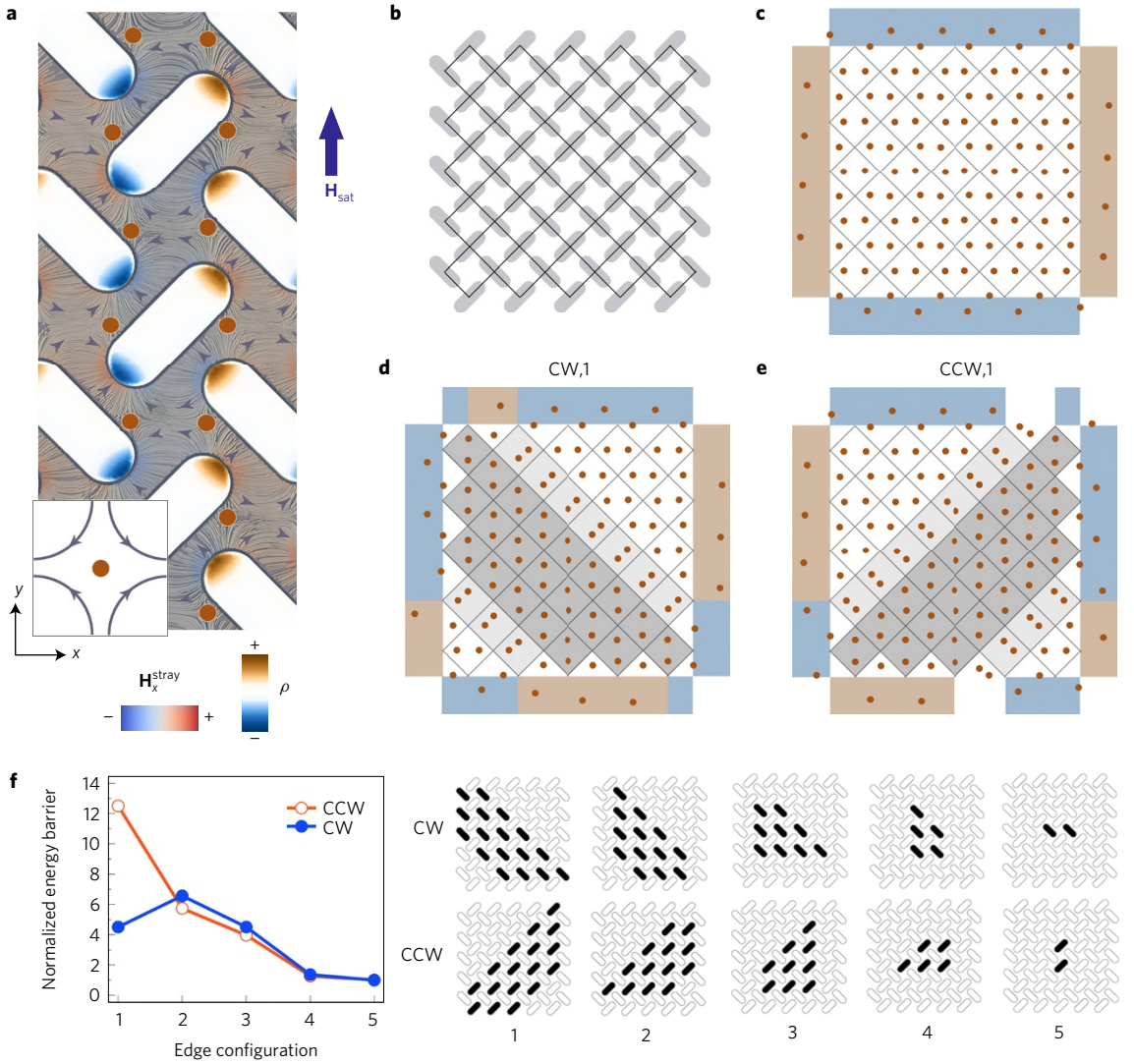

Figure 3 | Simulated stray field structure and energy barriers for clockwise and counterclockwise rotations of the average magnetization. a, Stray field configuration for a portion of the simulated nanomagnet array in state A, following saturation with the field $\mathbf{H}_{sat}$. The centres of the virtual antivortices are highlighted by orange dots and the magnetic volume charge density (ρ) within the single-domain nanomagnets is plotted using the blue–brown colourmap. The x component of the stray field, H_x^{stray}, is indicated by the blue–red colourmap. An antivortex structure is schematically shown in the bottom inset. **b**, Wire frame representation of the array lattice. **c**, Distribution of the virtual antivortices (orange dots) in the array in state A, following saturation along the $+y$ direction. The different antivortex distributions along the array edges are highlighted in red and blue. **d**, Virtual antivortex distribution for a configuration in which the net magnetization along four diagonals (dark grey regions) was rotated clockwise by 90° (state B). The corresponding magnetic state of the array is shown in **f**: configuration 'CW,1' (CW with edge configuration 1). **e**, Virtual antivortex distribution for a configuration in which the net vertex magnetization along four diagonals is rotated counterclockwise by 90°, corresponding to the magnetic state 'CCW,1' in **f**. In the white regions along the array edges in **e**, the stray field distribution is identical to the one in the bulk. **f**, Normalized energy barriers at 300 K, starting from the remanent state A (seen in **a**), to access the shown configurations 1–5 in which the reversal of the magnetization in edge nanomagnets is gradually set back (see Fig. 1 for colour convention indicating the orientation of the magnetization within nanomagnets). The energies are normalized to the barrier required to switch the two nanomagnets in the configurations labelled '5', where the barrier is the same for the CW and CCW rotations.

the sense of rotation of the net vertex magnetization. Indeed, after saturating a system with a nominally identical geometry to the one in Fig. 2 (see Methods) along the $-y$ direction (Fig. 4a) we observe that, in the presence of $\mathbf{H}_{bias}$, the thermal evolution can proceed through the counterclockwise rotation of the net vertex magnetization (Fig. 4b–d). Depending on the saturation direction, it is thus in principle possible to use a bias field to reinforce the 'built-in' clockwise rotation or to favour the counterclockwise sense of rotation of the average magnetization.

The magnetostatic interaction offers a known route for symmetry breaking at the surface of ferromagnets that can lead to rich behaviour, such as surface- and curvature-induced non-reciprocal spin wave[28,29] and domain wall[30,31] propagation. Similarly, in the studied artificial spin system, the origin of the thermally activated unidirectional rotation of the average magnetization is due to the dynamic rearrangement of emergent magnetic surface charges, which result from the geometry of the array edges, demonstrating how magnetostatically coupled nanomagnet arrays can be designed to harness thermal fluctuations of the magnetization. This opens the possibility of exploiting artificial spin ices with tailored edge geometry and field-tunable dynamics as functional, active materials within devices that convert heat into motion, such as mesoscopic motors[20,22] and rotors[32], or within hybrid multistacks, used for example for magnetic memory applications[33], where the chiral

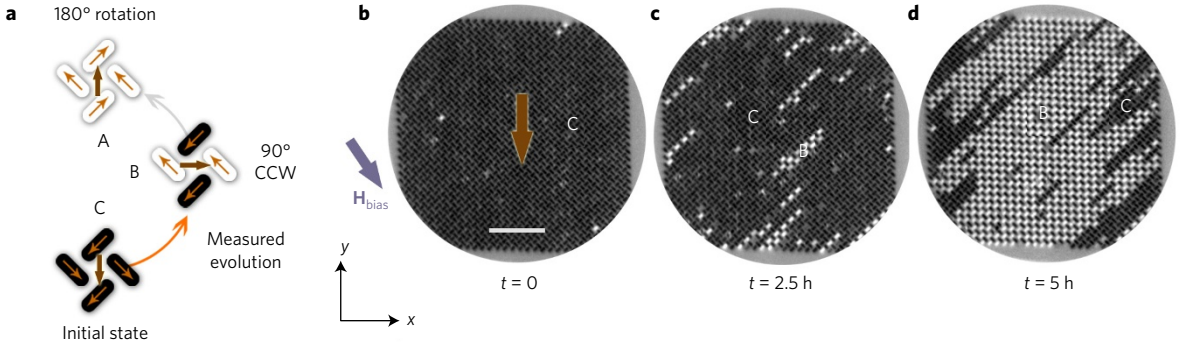

Figure 4 | Counterclockwise evolution of the system following saturation in the −*y* direction. a, After saturating the array along the −*y* direction, the magnetization evolves counterclockwise—that is, from state C to state B (orange arrow), in the presence of the bias field $\mathbf{H}_{bias}$. **b**–**d** Measured time evolution of the magnetization. In **b**, the array is in state C after saturation and the average magnetization is indicated by the large brown arrow. The evolution towards the sate shown in **c** occurs at room temperature. By heating the sample for 2.5 h, the state shown in **d** can be accessed. The rotation from state B to state A was not observed owing to the orientation of the bias field. We note that the counterclockwise rotation from state C to state B is observed in about 20% of the measured samples. Indeed, starting from state C, the counterclockwise evolution favoured by the bias field competes with the natural clockwise evolution of the system and can cause the array to remain, on average, in state C. The scalebar represents 5 μm.

array would form the active layer in which the rotation of the magnetization could be triggered by laser pulses.

Methods

Methods, including statements of data availability and any associated accession codes and references, are available in the online version of this paper.

Received 30 March 2017; accepted 12 September 2017; published online 25 October 2017

References

1. Wang, R. F. *et al*. Artificial 'spin ice' in a geometrically frustrated lattice of nanoscale ferromagnetic islands. *Nature* **439,** 303–306 (2006).
2. Heyderman, L. J. & Stamps, R. L. Artificial ferroic systems: novel functionality from structure, interactions and dynamics. *J. Phys. Condens. Matter* **25,** 363201 (2013).
3. Morrison, M. J., Nelson, T. R. & Nisoli, C. Unhappy vertices in artificial spin ice: new degeneracies from vertex frustration. *New J. Phys.* **15,** 045009 (2013).
4. Mengotti, E. *et al*. Real-space observation of emergent magnetic monopoles and associated Dirac strings in artificial kagome spin ice. *Nat. Phys.* **7,** 68–74 (2010).
5. Vedmedenko, E. Y. Dynamics of bound monopoles in artificial spin ice: How to store energy in Dirac strings. *Phys. Rev. Lett.* **116,** 077202 (2016).
6. Gilbert, I. *et al*. Emergent ice rule and magnetic charge screening from vertex frustration in artificial spin ice. *Nat. Phys.* **10,** 670–675 (2014).
7. Farhan, A. *et al*. Thermodynamics of emergent magnetic charge screening in artificial spin ice. *Nat. Commun.* **7,** 12635 (2016).
8. Branford, W. R., Ladak, S., Read, D. E., Zeissler, K. & Cohen, L. F. Emerging chirality in artificial spin ice. *Science* **335,** 1597–1600 (2012).
9. Le, B. *et al*. Understanding magnetotransport signatures in networks of connected permalloy nanowires. *Phys. Rev. B* **95,** 060405(R) (2017).
10. Gliga, S., Kákay, A., Hertel, R. & Heinonen, O. G. Spectral analysis of topological defects in an artificial spin-ice lattice. *Phys. Rev. Lett.* **110,** 117205 (2013).
11. Jungfleisch, M. B. *et al*. Dynamic response of an artificial square spin ice. *Phys. Rev. B* **93,** 100401(R) (2016).
12. Bhat, V. S., Heimbach, F., Stasinopoulos, I. & Grundler, D. Magnetization dynamics of topological defects and the spin solid in a kagome artificial spin ice. *Phys. Rev. B* **93,** 140401(R) (2016).
13. Kelly, T. R., De Silva, H. & Silva, R. A. Unidirectional rotary motion in a molecular system. *Nature* **401,** 150–152 (1999).
14. Mochizuki, M. *et al*. Thermally driven ratchet motion of a skyrmion microcrystal and topological magnon Hall effect. *Nat. Mater.* **13,** 241–246 (2014).
15. Gansel, J. K. *et al*. Gold helix photonic metamaterial as broadband circular polarizer. *Science* **325,** 1513–1515 (2009).
16. Bode, M. *et al*. Chiral magnetic order at surfaces driven by inversion asymmetry. *Nature* **447,** 190–193 (2007).
17. Zakeri, Kh. *et al*. Asymmetric spin-wave dispersion on Fe(110): direct evidence of the Dzyaloshinskii–Moriya interaction. *Phys. Rev. Lett.* **104,** 137203 (2010).
18. Barron, L. D. True and false chirality and parity violation. *Chem. Phys. Lett.* **123,** 423–427 (1986).
19. Hel-Or, Y., Peleg, S. & Avnir, D. Two-dimensional rotational dynamic chirality and a chirality scale. *Langmuir* **6,** 1691–1695 (1990).
20. Browne, W. R. & Feringa, B. L. Making molecular machines work. *Nat. Nanotech.* **1,** 25–35 (2006).
21. Romanczuk, P., Chaté, H., Chen, L., Ngo, S. & Toner, J. Emergent smectic order in simple active particle models. *New J. Phys.* **18,** 063015 (2016).
22. Hänggi, P. & Marchesoni, F. Artificial Brownian motors: controlling transport on the nanoscale. *Rev. Mod. Phys.* **81,** 387–442 (2009).
23. Kapaklis, V. *et al*. Thermal fluctuations in artificial spin ice. *Nat. Nanotech.* **9,** 514–519 (2014).
24. Farhan, A. *et al*. Exploring hyper-cubic energy landscapes in thermally active finite artificial spin-ice systems. *Nat. Phys.* **9,** 375–382 (2013).
25. Gliga, S., Hertel, R. & Schneider, C. M. Switching a magnetic antivortex core with ultrashort field pulses. *J. Appl. Phys.* **103,** 07B115 (2008).
26. Dotse, D. & Arrott, A. S. Micromagnetic studies of vortices leaving and entering square nanoboxes. *J. Appl. Phys.* **97,** 10E307 (2005).
27. Kumar, D., Barman, S. & Barman, A. Magnetic vortex based transistor operations. *Sci. Rep.* **4,** 4180 (2014).
28. Camley, R. E. Nonreciprocal surface waves. *Surf. Sci. Rep.* **7,** 103–187 (1987).
29. Otálora, J. A., Yan, M., Schultheiss, H., Hertel, R. & Kákay, A. Curvature-induced asymmetric spin-wave dispersion. *Phys. Rev. Lett.* **117,** 227203 (2016).
30. Yan, M., Andreas, C., Kákay, A., Garcia-Sanchez, F. & Hertel, R. Chiral symmetry breaking and pair-creation mediated Walker breakdown in magnetic nanotubes. *Appl. Phys. Lett.* **100,** 252401 (2012).
31. Hertel, R. Curvature-induced magnetochirality. *SPIN* **03,** 1340009 (2013).
32. Fletcher, S. P., Dumur, F., Pollard, M. M. & Feringa, B. L. A reversible, unidirectional molecular rotary motor driven by chemical energy. *Science* **310,** 80–82 (2005).
33. Wong, H.-S. P. & Salahuddin, S. Memory leads the way to better computing. *Nat. Nanotech.* **10,** 191–194 (2015).

Acknowledgements

The authors thank O. Sendetskyi, H. Arava, V. Guzenko, E. Deckardt and J. Bosgra for technical assistance. S.G. wishes to thank N. Leo and A. S. Arrott for helpful discussions as well as S. Arnold for advice on the graphics in the manuscript. R.L.S. thanks F. Nascimento for discussions. S.G. was funded by the European Union's Horizon 2020 research and innovation programme under the Marie Sklodowska-Curie grant agreement no. 708674. The work of G.H. was supported by the EPSRC (grants EP/M015173/1 and EP/L019876/1), the Vienna Science and Technology Fund under WWTF Project MA14-44 and the Royal Society under Grant No. UF080837. The work of R.L.S. was supported by the EPSRC (grants EP/ L002922/1 and EP/M024423/1). This work was supported by JSPS Core-to-Core Program, A. Advanced Research Networks. A.F. was supported by the Swiss National Science Foundation. Part of this work was performed at the Surface/Interface: Microscopy (SIM) beamline of the Swiss Light Source, Paul Scherrer Institut, Villigen, Switzerland. This research used resources of the Advanced Light Source, which is a DOE Office of Science User Facility under contract no. DE-AC02-05CH11231. Use of the Center for Nanoscale Materials, an Office of

Science user facility, was supported by the US Department of Energy, Office of Science, Office of Basic Energy Sciences, under Contract No. DE-AC02-06CH11357.

Author contributions

R.L.S. and S.G. conceived the spin ice geometry and the experiment. S.G., A.F., C.D. and J.C. prepared the samples. S.G., C.D., J.C., J.B., A.K., A.F., R.V.C., E.K., A.S. and N.S.B. performed the experiments and analysed the experimental data. G.H., S.G. and J.B. performed and evaluated the micromagnetic simulations. S.G., G.H., R.L.S., J.B., C.D., A.K., Y.M. and L.J.H. interpreted the results. S.G. wrote the manuscript with input from all coauthors. All authors discussed the results and commented on the manuscript.

Additional information

Supplementary information is available in the online version of the paper. Reprints and permissions information is available online at www.nature.com/reprints. Publisher's note: Springer Nature remains neutral with regard to jurisdictional claims in published maps and institutional affiliations. Correspondence and requests for materials should be addressed to S.G.

Competing financial interests

The authors declare no competing financial interests.

Methods

Sample fabrication. Finite arrays of Permalloy ($Ni_{83}Fe_{17}$) nanomagnets were prepared on a silicon (100) substrate using electron beam lithography in conjunction with thermal evaporation at room temperature and a base pressure of 2×10^{-7} mbar followed by lift-off. The evaporation resulted in a nanocrystalline Permalloy film, which was capped by a 3 nm aluminium layer to protect against oxidation. The Permalloy film was evaporated with a thickness gradient along the sample to ensure the presence of a thermally active region at room temperature adequate for the PEEM measurements[24]. Array thicknesses were measured using atomic force microscopy (AFM). The thermally active arrays in Figs 2 and 4 had identical layouts and were manufactured from nanomagnets with a length of 470 nm and a width of 170 nm, and with a lattice constant of 425 nm (centre-to-centre distance of neighbouring nanomagnets: see Supplementary Information 1 for the definition of the lattice constant). The measured thickness of the arrays was 2.2 nm in Fig. 1 and 2.7 nm in Fig. 4. The thicknesses were uniform across each array. The magnetization in both arrays rotated clockwise after saturating along the $+y$ direction, demonstrating that the thickness variation between the arrays did not affect the sense of rotation of the magnetization. The array in Supplementary Information 4 had a thickness of 2.4 nm. The chiral structure of the system is defined by the geometry of the array edges as well as by its two-dimensional character, where the shape anisotropy induced by the low Permalloy thickness ensures that the magnetization is confined to the plane of the sample.

Experiment. Magnetic imaging was carried out with the photoemission electron microscopy endstation[34] at the Surface/Interface: Microscopy (SIM) beamline of the Swiss Light Source, Paul Scherrer Institute and at the PEEM-3 photoemission electron microscope at beamline 11.0.1 of the Advanced Light Source, Berkeley National Laboratory. Employing XMCD, the system was imaged by tuning the X-ray energy to the Fe L_3-edge. The magnetic contrast images were obtained by pixelwise division of two consecutive images recorded with right and left circular polarizations. The resulting contrast is proportional to $\mathbf{k} \cdot \mathbf{M}$, where $\mathbf{k}$ is the propagation vector of the X-rays and $\mathbf{M}$ the magnetization[35]. The sample orientation was optimized to maximize the contrast. The uniform contrast within the nanomagnets indicates that they were in a single-domain state. Nanomagnets with grey contrast were switching faster than the measurement time. For observations of the magnetization reversal at the Swiss Light Source, the samples were mounted on a copper (nonmagnetic) holder that allowed radiative heating of the sample, and the temperature was measured using a PT100 sensor placed close to the sample. During the experiments the sample was exposed to a small constant bias field with an estimated in-plane magnitude $\mu_0 H_{\mathrm{bias}}$ of 50–80 μT based on Hall probe measurements. The arrays were saturated *in situ* using a permanent magnet inserted into the PEEM chamber. The saturating field strength at the location of the sample was $\mu_0 H_{\mathrm{sat}} = 15$ mT in the plane of the sample. The magnet was retracted from the chamber after saturation. Measurements at the Advanced Light Source were carried out by saturating the sample both *ex situ* as well as in a holder with a built-in electromagnet, which allowed us to apply fields up to 20 mT.

Micromagnetic simulations. Fully three-dimensional micromagnetic simulations based on a hybrid finite-element/boundary-element method[36] have been carried out on a system of 60 nanomagnets, each with lateral dimensions 235 nm × 85 nm (50% of experimental size) and 2 nm thick. The structure was discretized using a tetrahedral mesh with an average edge length of 1 nm. The material parameters for Permalloy were: saturation polarization $\mu_0 M_S = 1$ T, exchange constant $A = 1.3 \times 10^{-11}$ J m^{-1} and zero magnetocrystalline anisotropy $K = 0$. The total Gibbs magnetic free energy is given by

$$E(\mathbf{m}) = \int \left(A \left[\sum_k^{x,y,z} (\nabla m_k)^2 \right] + K[1 - (\mathbf{m} \cdot \mathbf{a})^2] - \frac{1}{2} \mu_0 M_S (\mathbf{H}_{\mathrm{dem}} \cdot \mathbf{m}) - \mu_0 M_S (\mathbf{H}_{\mathrm{ext}} \cdot \mathbf{m}) \right) \mathrm{d}V \quad (1)$$

where E is the sum of the exchange energy, the anisotropy energy, the demagnetizing energy, and the Zeeman energy. $\mathbf{m} = \mathbf{M}/M_S$ is the reduced magnetization, A is the exchange constant, K the magnetocrystalline anisotropy, $\mathbf{a}$ is a unit vector along the magnetocrystalline anisotropy direction, $\mathbf{H}_{\mathrm{dem}}$ is the demagnetizing field and $\mathbf{H}_{\mathrm{ext}}$ an external field. The integral is over the magnetic volume. In the performed simulations $H_{\mathrm{ext}} = 0$.

To understand the thermal stability and transition probability from the remanent state, following the application of a saturating field, to different magnetic states—that is, configurations resulting from clockwise and counterclockwise rotations, we used the nudged elastic band method to find the lowest possible energy transition path between the two states[37]. We start from a magnetization state, $\mathbf{M}_1$, where the magnetic system occupies a local energy minimum. Through thermal activation the system can overcome the local energy barrier and move towards a different minimum state, $\mathbf{M}_2$, following either clockwise or counterclockwise rotation of the vertex magnetization. The difference between the local energy minima and the saddle point in the energy path gives the energy barrier that has to be overcome to move to the next local minima; this determines the stability of the magnetic state. An optimization algorithm is applied until, at any point along the path, the gradient of the energy is pointing only along the path. This represents the path with the greatest statistical weight. The state with the lowest energy barrier has the highest probability of being reached.

Data availability. The data that support the findings of this study are available from the corresponding author S.G. upon reasonable request.

References

34. Le Guyader, L. *et al*. Studying nanomagnets and magnetic heterostructures with X-ray PEEM at the Swiss Light Source. *J. Electron Spectrosc. Related Phenom.* **185,** 371–380 (2012).
35. Stöhr, J. *et al*. Element-specific magnetic microscopy with circularly polarized X-rays. *Science* **259,** 658–661 (1993).
36. Chantrell, R. W., Fidler, J., Schrefl, T. & Wongsam, M. *Encyclopedia of Materials: Science and Technology* Micromagnetics: finite element approach. 5651–5660 (Elsevier, 2001).
37. Dittrich, R. *et al*. A path method for finding energy barriers and minimum energy paths in complex micromagnetic systems. *J. Magn. Magn. Mater.* **250,** L12 (2002).